Ceramics International 49 (2023) 25788–25794

Contents lists available at ScienceDirect

Ceramics International

journal homepage: www.elsevier.com/locate/ceramint

Estimation of thermal barrier coating fracture toughness using integrated computational materials engineering

Xibo Geng [a,b], Richard Wellman [c], Luis Isern Arrom [a], Christine Chalk [a], Gustavo M. Castelluccio [a,*]

[a] School of Aerospace, Transport and Manufacturing, Cranfield University, Bedfordshire, UK
[b] Siemens, UK
[c] Innio, Jenbach, Austria

ARTICLE INFO

Handling Editor: Dr P. Vincenzini

Keywords:
EB-PVD TBC
Foreign object damage
Ceramic fracture toughness
TBC fracture mechanics
Finite element analysis
TBC kink-Bands
And alumina interface fracture

ABSTRACT

The fracture toughness of thermal barrier coatings (TBC) is a critical mechanical property that governs damage resistance. Catastrophic delamination of TBC under erosion conditions occurs in TBC with low toughness. Prior research has explored indirect and complex experiments to measure TBC toughness, but the miniaturized nature of the multi-layered coating makes it difficult to quantify its intrinsic toughness. This paper integrates computational modeling and experimental approaches to estimate the TBC toughness and the substrate delamination strength. The results show that a typical newly fabricated yttrium stabilized zirconia coating under service conditions has a toughness estimated in the range of 0.1–0.5 MPa $m^{1/2}$ and a toughness of thermally grown oxide layer in between 1.5 and 1.7 MPa $m^{1/2}$. The analysis also determined that a thermally grown oxide with a fracture toughness above 2.0 MPa $m^{1/2}$ would not delaminate under the service conditions. Overall, the approach demonstrates the value of integrated computational material approaches, which can save time and enhance predictive power.

1. Introduction

Aeroengine manufacturers require modern gas turbines to operate at increasingly higher temperatures to reduce CO_2 emissions and achieve better fuel efficiency. Thermal Barrier Coatings (TBCs) (Fig. 1 a) are a critical material solution that offers thermal insulation in the hottest engine sections, allowing them to work at higher temperatures and for a longer lifespan. A typical TBC system consists of three layers as shown in Fig. 1 b). A ceramic Top Coat (TC), an active Thermally Grown Oxide (TGO) layer that thickens with the engine aging, and a metallic Bond Coat (BC). TCs are normally manufactured using Electron Beam Physical Vapour Deposition (EB-PVD) on rotating turbine components such as the high-pressure turbine blade in Fig. 1 a). Ceramic structures are separated by inter-columnar gaps and feathery structures that result from secondary grain growth (Fig. 2). Columnar TBCs offer high damage tolerance, which is required by high thermal cyclic applications [1].

During service, TBCs are subjected to chemical degradation (e.g., oxidation, corrosion, etc) and mechanical erosion from the impact of airborne particles ingested by the engine. Currently, industry standard TBC corresponds to 7 wt% yttrium stabilized zirconia (7YSZ) [1] and attempts to introduce new materials resulted in poor erosion resistance due to the apparent lower fracture toughness [2–4]. Therefore, identifying TBC toughness becomes a critical aspect to ascertain erosion resistance and predict TBC service life in an erosive environment.

The small thickness of TBCs and the heterogeneity of their structure prevent the implementation of standardized fracture toughness testing. Hence, TBC toughness has often been indirectly estimated by indentation methods [5], which are time-consuming, ambiguous, and sometimes unavailable (e.g., at high temperatures and high deformation rates). Indeed, prior approaches rely on multiple assumptions to justify a closed correlation among observable quantities (local stress, penetration depth, and energy applied) with toughness. As a result, toughness estimation may be unreliable and may have significant uncertainty, especially when extrapolated to service conditions.

Prior computational efforts [6,7] have compared the response of TBC with experiments to study different material and microstructural effects during thermal cycling. However, only a few approaches have focused on structure-sensitive approaches capable of estimating the coating

* Corresponding author.
E-mail address: castellg@cranfield.ac.uk (G.M. Castelluccio).

https://doi.org/10.1016/j.ceramint.2023.05.124
Received 13 February 2023; Received in revised form 9 May 2023; Accepted 14 May 2023
Available online 15 May 2023

toughness. Hence, we present substructure-sensitive finite element simulations (FEM) with columnar multi-layered microstructure to quantify TBC toughness by comparing simulation results with foreign object damage (FOD) experimental observations. This approach identifies various observable indicators that are employed to characterize toughness and delamination resistance at high temperatures and high strain rates. The results present a novel solution to estimate the mechanical response of TBCs under realistic service conditions.

1.1. Experimental characterization

TBC samples were fabricated on a 1.6 mm thick Nimonic 75 substrate with a NiAl bond coat deposited by Chemical Vapour Deposition and a top coat of 7YSZ deposited by EB-PVD using a Von Ardenne EBE150 system. Samples were tested in an erosion rig schematically depicted in Fig. 3, which simulates FOD from millimeter-sized particles impacting turbine blades TBC at speeds above 100 m/s [8,9]. The rig directs hot gas at 1000 °C towards samples to reach typical TBC service temperatures of 800–880 °C. A total of 0.1 g Honite particles with a diameter between 700 μm and 850 μm were added to the airstream to impact the TBC sample at high speed. Prior experimental efforts [10,11] have demonstrated that this method results in damage mechanisms and extensions similar to those suffered by turbine engines during service. Moreover, the rig allows one to measure and control precisely the environment at a fraction of the cost of running a real engine.

Fig. 4 exemplifies the damage induced by the erosion rig on a TBC sample. Fig. 4 a) corresponds to the top view of the TBC while Fig. 4 b) presents a scanning electronic microscopy (SEM) image of the sample cross-section, which was cut and polished along the highlighted line. The average impact penetration depth (δ_{max} in Fig. 4 b) measured from cross-section images is a key damage indicator of TBC FOD as shown in previous studies [13–16].

1.2. Modeling approach

FEM models in Abaqus/CAE 2022 were implemented to conduct Dynamic/Explicit analysis that simulates the FOD impact on TBC. The models shown in Fig. 5 consist of a 1 mm thick substrate covered with three layers: TC, TGO, and BC with a thickness of 170 μm, 1 μm, and 25 μm, respectively; the TGO thickness corresponds to a pristine coating that has not been aged. Experiments [13,14] suggest that FOD results in an affected area with a typical radius of 350 μm. Therefore, the TBC model employs a sample side length of 1 mm as shown in Fig. 5. Furthermore, the FOD particle corresponds to a rigid ball 850 μm in diameter and an impact speed of 100 ms^{-1}, which agrees with experiments to model the expected highest velocity.

Both 2D and 3D models depict a simplified TC composed of columnar beams with a 1 μm inter-columnar gap. The 2D model in Fig. 5 (a) employs quadratic elements to represent rectangular 10 μm columnar TC and continuous TGO with a mesh size of 5 μm, while the BC and the substrate have 4 μm and 25 μm mesh size, respectively. Both models have the same boundary conditions, in which the TBC is fixed at the substrate bottom and pinned supported at the edges of the modeled sample.

The 3D model in Fig. 5 (b) employs a mesh size of 6.8 μm for the columnar TC and TGO, 12.5 μm for the BC, and 25 μm for the substrate. The TC corresponds to a 3D array of square-shaped cross-section columns with a constant inter-columnar gap. Compared to the TBC microstructure in Fig. 2, feather arms and intra-columnar porosity have not been explicitly represented in the models for simplification. Instead, a Coulomb friction model captures intercolumnar and top surface-ball interactions.

1.3. Material attributes

Much of the inelastic response of TBCs comes from the progressive compactification of the TC, which lacks significant strain hardening mechanisms. Hence, we proceed by approximating the TC response as an elastic-perfectly plastic response, which has often been used to represent compactification [17,18]. This model corresponds to a linear elastic response up to the yield stress, after which the stress remains constant with further straining. As demonstrated by Matsuzawa et al. [19], the yield stress of 7YSZ ceramics (σ_Y) is strain-rate dependent. Given that experiments [13] have shown that TC and BC experience strain rates of about 10^6 s^{-1} around the impact crater, the models should convey strain-rate effects. Hence, we employ a yield stress constitutive model with a power law dependence [13,20] on the strain rate,

$$\sigma_Y(\dot{\varepsilon}) = \sigma_Y(0)\left[1 + \left(\frac{\dot{\varepsilon}}{C}\right)^{\frac{1}{P}}\right] \quad (1)$$

in which $\sigma_Y(0)$ is the quasistatic yield stress, $\dot{\varepsilon}$ corresponds to the instantaneous strain rate while C and P are material parameters related to the Johnson-Cook rate dependence model [21]. The unavailability of high strain-rate related data for zirconia makes it difficult to precisely calibrate the material yield stress at a high strain rate. Instead, we mimic the response of AlN ceramics [22], for which the dynamic yield stress is approximately three times its quasi-static yield stress. Thus, as a first-order approximation we assume that zirconia has a similar response to AlN ceramics and we employed a multiplication factor of three to characterize TC and BC yield stresses at a high strain rate.

During FOD experiments, the sample temperature is on average at 840 °C, at which the fracture stress of TGO ($\sigma_{Debonding}$) is approximately 100 MPa according to the fracture map of alumina [23]. By further assuming that a strain rate multiplication factor of three applies to $\sigma_{Debonding}$, we estimate the fracture stress of alumina under testing conditions to be approximately 300 MPa [4].

The FOD particle is modeled as an elastic ball that does not break during impact. Given the lack of data, the yield stress of the TGO is approximated by that of the TC without any significant effect due to the relatively small thickness of the TGO. Table 1 presents the material properties, which were estimated from experimental data at high temperatures. We highlight that we will proceed with the analysis assuming these are independent parameterizations and we will perform a sensitivity analysis rather than calibrating the parameters to match exactly our experimental results.

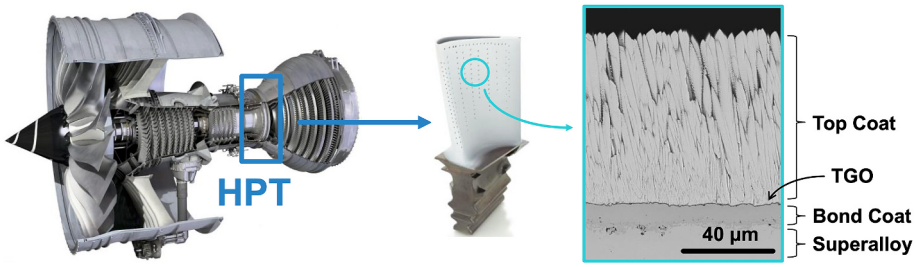

Fig. 1. Turbine blade in aero-engine cutaway and TBC SEM image detailing EB-PVD TBC structure.

1.4. TGO cohesive contact

The delamination between the TGO and the BC is evaluated with a cohesive contact model shown in Fig. 6 a). The cohesive contact model is defined by the traction-separation law in Fig. 6 b) [6], which is characterized by the three parameters: elastic behavior of the cohesive contact represented by modulus (K), damage initiation stress level ($\sigma_{Debonding}$), and fracture energy (G_C) defined by the area under the curve. As demonstrated next, we considered an integrated engineering approach that validates these parameters based on the debonded crack length observed on experimental samples.

2. Modeling results

2.1. Parameter sensitivity analysis

Given the experimental difficulties in identifying material constants, we proceed with a sensitivity analysis running 2D and 3D simulations with small changes to the parameters in Table 1. For each simulation, we quantified the impact penetration depth, which is a useful indicator of FOD damage. Fig. 7 presents the penetration depth (δ) calculated with 2D models using ranges for the values of the TC density (ρ^{TC}), Young's modulus (E^{TC}), Poisson's ratio (v^{TC}), static yield stress (σ_Y^{TC}), thickness (h^{TC}), inter-columnar gap (g), friction coefficient of the top TC surface (μ_P) and friction coefficient of the column edge surface (μ_C). The results in Fig. 8 demonstrate that density and elastic properties have a minimal effect on the FOD penetration depth; hence, the role of the feather crystal orientation in affecting FOD is secondary. The column edge friction coefficient and the inter-columnar gap affect the penetration by about 10%–30%, respectively, which agrees with the results by Wang et al. [5] despite assuming a bilinear kinematic hardening model. Finally, the yield stress affects the most penetration prognosis, but an increase in yield strength of 500% only changes the penetration by 40%.

Next, we considered the sensitivity to particle diameters between 700 and 850 μm and impact velocity between 50 and 100 m/s at 900 °C. In this case, we employ inter-columnar gaps of 1 μm and a static yield stress of TC is 180 MPa with a multiplication factor of three for the strain-rate-dependence. Fig. 7 summarizes the FOD penetration depths from five experimental samples using 2D and 3D models. These results show a surprisingly close match between models and experiments, even when considering independent best estimates for some material properties. Thus, model input uncertainty is not detrimental enough to affect the model predictive power of the penetration depth, which is related to kink bands and delamination inside TBC [13–16].

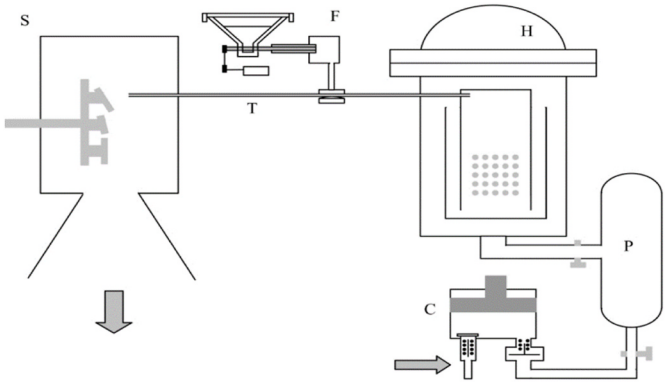

Fig. 3. Schematics of erosion rig – furnace (H), gas tube (T) connecting furnace and TBC sample chamber (S), erosion particle feeding device (F) [9,12].

2.2. Kink bands and crack indicators

Given the brittle nature of TBC, the maximum principal stress is a natural damage indicator parameter for the potential of crack initiation. Indeed, the red stress concentrated zones shown in Fig. 9 closely resemble the experimental kink bands in Fig. 4. The kink-band-like field corresponds to tensile stresses that arise from the bending of the columns and highlight the value of representing the TBC substructure. The results present a compactification zone right under the impact point, continued by a kink band with a chevron pattern in the range of 45–90 MPa for a 2D model.

Fig. 10 a) depicts the 3D model along with SEM images from a FOD experiment sample. Both models and experiments develop similar compaction zones underneath the top surface around the impact center, which gradually reduces as the cross-section moves away from the center. At the cross-section in the medium point between the impact center and the crater edge (Fig. 10b), there is no compaction, but cracks have developed underneath the top surface in the middle area. These cracks correlate with the location of the maximum principal stresses in TC (60–90 MPa), which is taken as the critical stress to crack the column. The maximum principal stress depicts a chevron crack pattern (kink-band) from the bending of the columns. Notably, for similar impact speed, columns in 3D models become less bent compared to bending in 2D.

At the impact center and the medium position in Fig. 10a/b, severe cracking occurs at kink bands. SEM images show the kink bands start

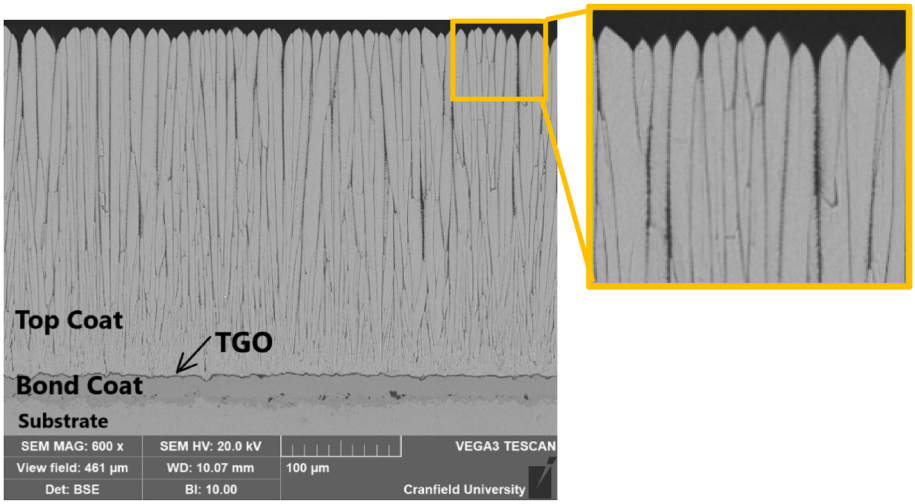

Fig. 2. SEM image of TBC cross-section and zoomed view of the top coat column's feathery edges shown in the yellow circle. (For interpretation of the references to colour in this figure legend, the reader is referred to the Web version of this article.)

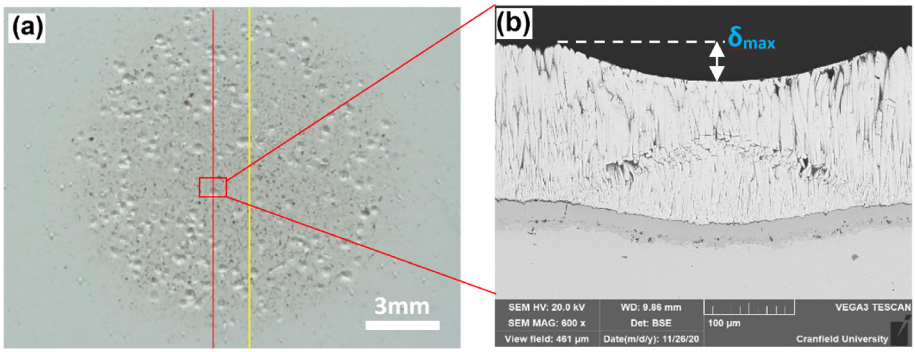

Fig. 4. (a) Top-view of a damaged TBC sample with yellow cut line and red polish line, (b) SEM image of TBC cross-section under crater at the highlighted red area, note the kink-band on the TBC. (For interpretation of the references to colour in this figure legend, the reader is referred to the Web version of this article.)

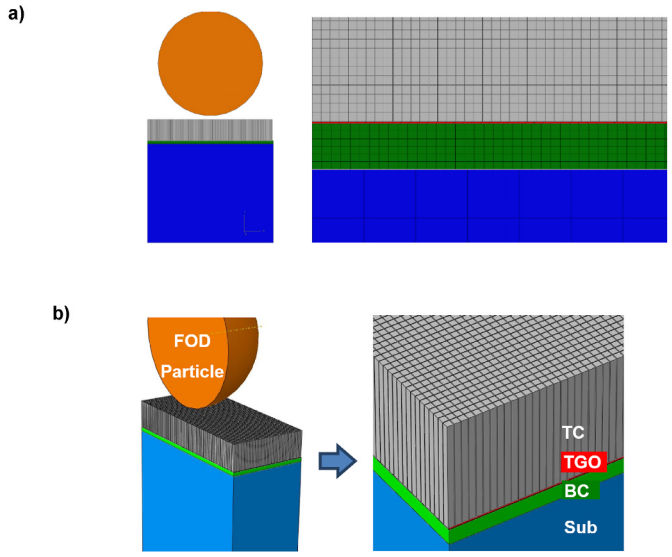

Fig. 5. FEM models represent a foreign object impacting a TBC with three layers. (a) 2D model, (b) 3D model. Note both the 2D and 3D models have employed the array of continuous columns to represent the EB-PVD TBC columnar microstructure.

from the middle of the TC and propagate towards the TGO. The 3D model shows similar patterns by painting red elements with principal stress between 60 and 90 MPa. In Fig. 10, cracks near the crater boundary are also found in the SEM image. These cracks are not as open as in the kink bands and they are around the circular crater boundary near the top surface. The 3D model also shows several red elements with

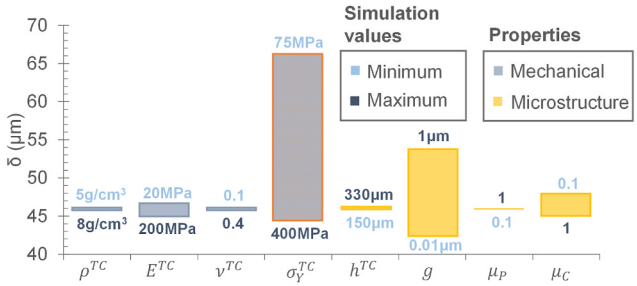

Baseline Value	5.9	62	0.25	180	170	1	0.5	0.5
Change with an approx interval	1	20	0.05	25	20	0.1	0.1	0.1

Fig. 7. Effects of each TC property on FOD penetration depth (δ) quantified with the 2D model sensitivity tests with FOD particle of 850 μm diameter impacting at 100 m/s. Properties changed one at a time within an interval of change noted in blue. (For interpretation of the references to colour in this figure legend, the reader is referred to the Web version of this article.)

Table 1
TBC model material characterisations [13,24–28].

	Material	Density (kg/m^3)	Young's modulus (GPa)	Poisson's ratio	Yield stress (MPa)	Strain-rate dependent yield stress (MPa)
FOD Particle	Honite at room temp	1500	72	0.23	N/A	N/A
TC	7YSZ at 900 °C	5900	62	0.25	180	X3 = 540
TGO	Alumina at 800 °C	3500	325	0.25	180	540
BC	NiAl at 800 °C	5900	110	0.31	120	X3 = 360
Substrate	Nimonic 75 at 800 °C	8360	165	0.3	190	N/A

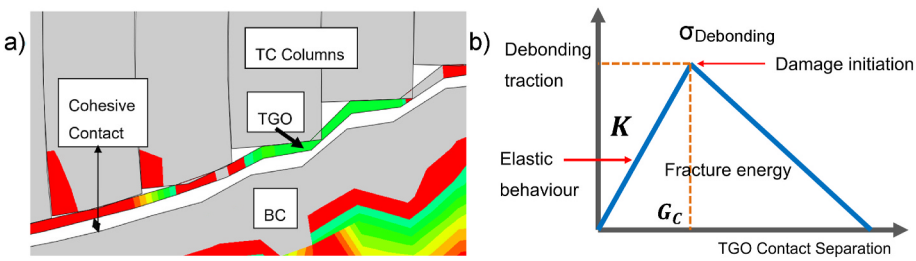

Fig. 6. a) 2D Model FOD simulation shows the separation of TC/TGO from BC governed by the cohesive contact applied between TGO and BC. b) Traction-separation law of cohesive contact [6].

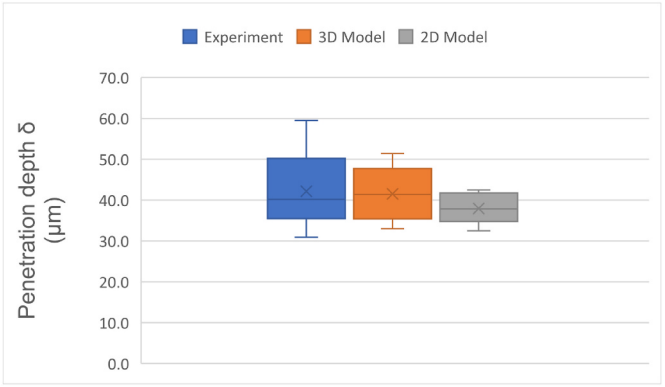

Fig. 8. Effects of Honite particle diameter (700–850 μm) and speed (50–100 m/s) on FOD penetration depth (δ) compared between experiment samples, 2D and 3D FEM models, showing a close match.

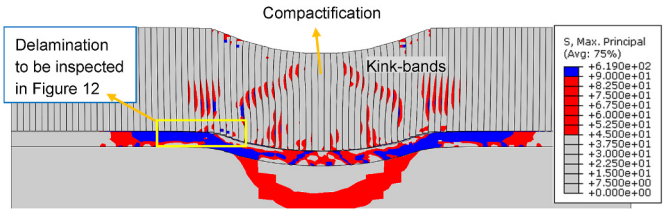

Fig. 9. Maximum principal stress computed with a 2D model of TBC after the impact of a spherical rigid particle with a diameter of 850 μm and speed of 100 m/s (units in MPa).

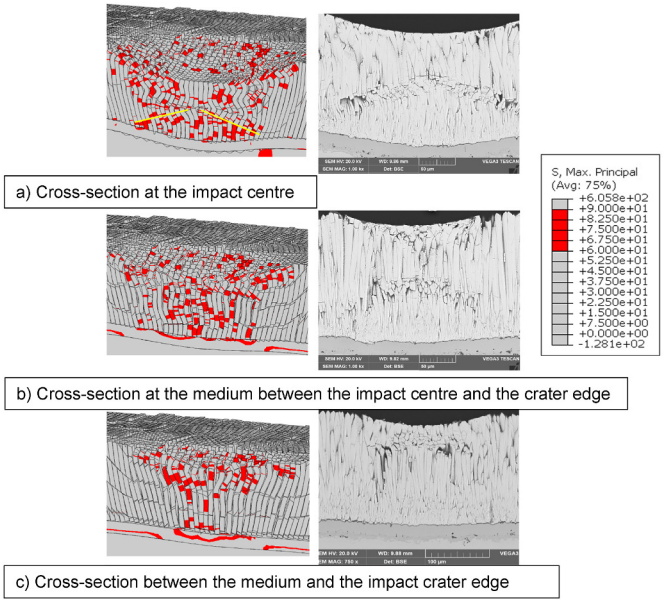

Fig. 10. Comparisons of 3D model prediction with experimental SEM image of the three cross-sections located across the impact crater.

local principal stresses in the range of 60–90 MPa around the circular crater boundary in Fig. 10.

2.3. Estimation of TGO interface delamination fracture energy

Our sensitivity analysis shows that simple material models and independent estimations of material properties carry good intrinsic predictive power for particle penetration and kink band formation. Indeed, several researchers have modeled particle penetration and supported the use of simple models to quantify complex attributes such as fracture toughness and delamination [29].

The cohesive contact model between TGO and BC is governed by the three parameters, K, G_C, and $\sigma_{Debonding}$ as defined in Fig. 6 b). Since the TGO is a thin (1 μm) layer formed by alumina (α-Al2O3), the elastic behavior of TGO is governed by Young's modulus of TC, which is estimated to be 62 GPa at 900 °C [26]. The peak (debonding) stress $\sigma_{Debonding}$ is about 100 MPa according to the transcrystalline cleavage fracture stress of alumina at 800 °C [23]. After inspecting the sample, the longest TGO delamination crack length is approximately 120 μm, as shown in Fig. 11.

We can estimate the fracture energy by assuming that the longest delamination crack was caused by a ball with the largest diameter (850 μm) traveling at the fasted speed (100 m/s). Hence, we performed a sensitivity study with the 2D model, assuming a range of fracture energies and computing the corresponding TGO interface delamination length as shown in Fig. 12. The results in Fig. 13 demonstrate that a decrease in fracture energy increases the delamination crack length. The experimental observation in Fig. 11 with a 120 μm crack corresponds to a fracture energy G between 35 Jm^{-2} to 45 Jm^{-2} as shown in Fig. 13. These results agree with prior reports [5], which estimated the fracture energy to be about 20 Jm^{-2} to 38 Jm^{-2} for TBC samples after 35 thermal cycles. Since our samples were newly fabricated and had not been aged, we would expect their fracture energy to be higher.

2.4. Kink-bands crack analysis and TC fracture toughness

The simulations suggest that the minimum crack initiation tensile stress is 45 MPa and 60 MPa for 2D and 3D models, respectively. Hence, we can estimate the tensile stress required to fracture the TC is in the range of 45–90 MPa. Following linear elastic fracture mechanics, the critical stress intensity factor (K_{IC}) of a sharp crack can be computed by,

$$K_{IC} = \sigma\sqrt{\pi a}\, f(a/W). \quad (2)$$

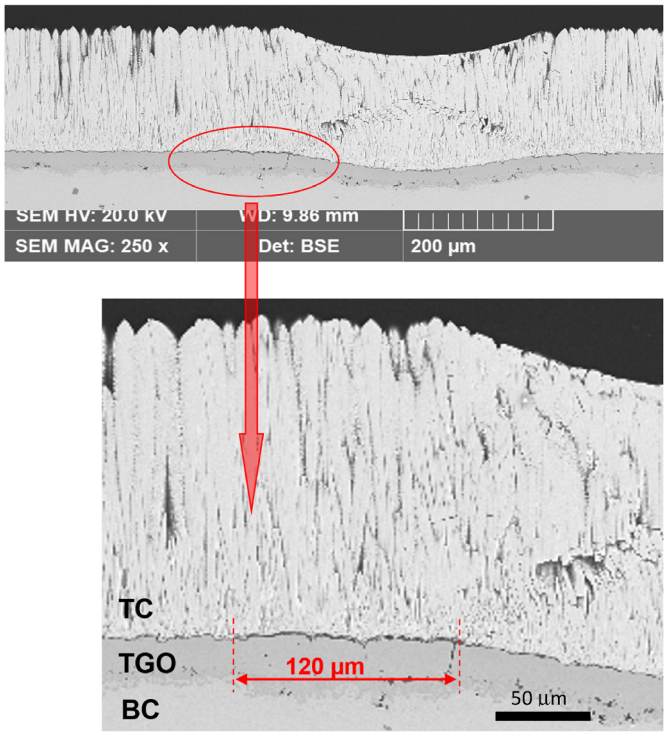

Fig. 11. Experiment measurement of the maximum length of delamination occurred at the TC/TGO or TGO/BC interfaces at one side of the TBC.

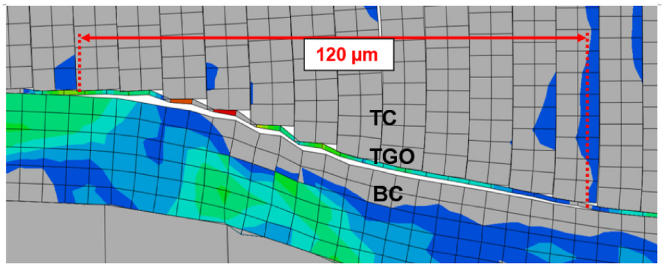

Fig. 12. Detail of the simulated delamination crack matching the experimental results in Fig. 9. The results suggest that the fracture energy G is between 35 Jm^{-2} to 45 Jm^{-2}

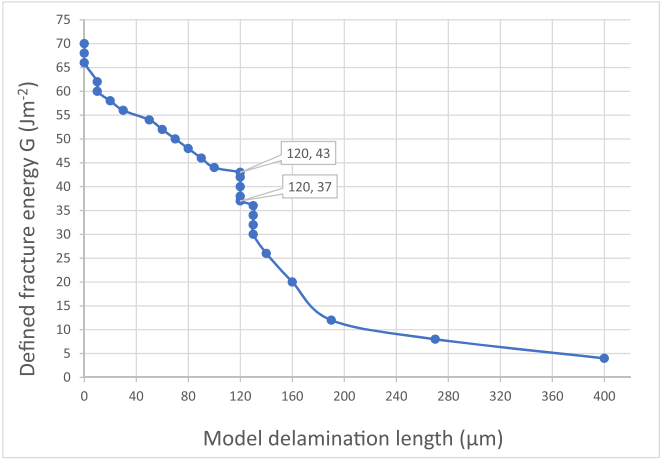

Fig. 13. TBC delamination length (on one side) predicted by the 2D model with different fracture energies (G), different values of G can result in the same delamination length because of the discrete nature of the mesh.

Following the critical stress computed with simulations, we assume stress σ = 45–90 MPa, geometry factor f(a/W) = 1.122 [30], and an initial crack length (*a*) between 2–7 μm as measured in Fig. 14. The resulting K_{IC} is between 0.1–0.5 MPa $m^{1/2}$, which agrees with Evan's estimation of YSZ mode-I fracture toughness between $0.1 \leq K_{IC} \leq 1$ MPa $m^{1/2}$ [20,26]. Thus, we demonstrate that simulations, FOD experiments, and material characterization can be effectively integrated to identify the crack initiation stress and TC Mode-I fracture toughness.

2.5. Estimation of the TGO interface fracture toughness

The fracture energy can also be related to the critical stress intensity factor,

$$G_C = (K_{IC})^2/E, \quad (3)$$

along with the TC Young's modulus to compute the critical fracture toughness of the delamination at the alumina interface. Following our calculation of G_C, the fracture toughness of the TGO alumina interface at 800 °C is estimated as $K_{IC} = 1.5–1.7$ MPa $m^{1/2}$. The fracture toughness of TGO has not been reported in the existing literature, but measurements of plasma-sprayed alumina coatings using indentation resulted in 0.5–2.5 MPa $m^{1/2}$ depending on manufacturing routes [31]. By comparison, our estimated range of TGO fracture toughness lies within the experiment-measured range of toughness of alumina coating, thus the estimation can be considered reasonable.

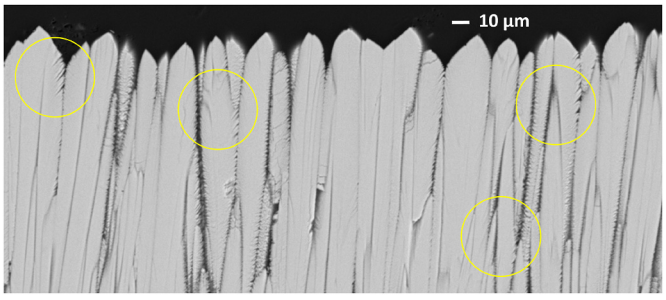

Fig. 14. TC SEM image showing the micro-cracks on column edges.

3. Discussion

The measurement of mechanical properties in TBCs is a challenging task given their small dimensions and complex microstructures. Rather than solely relying on costly and time-consuming coating indentation experiments, we have presented a blended approach that integrates information from various sources. We implemented finite element models and sensitivity analyses to identify the material properties that most affect particle penetration and coating delamination. The independent identification of these properties mitigated model input errors while models were further validated by comparing penetration depths and cracking patterns from experiments. Our integrated computational materials engineering approach offers the benefit that the uncertainty of the results can be further characterized and reduced with additional experimental testing and characterization. In addition, by analyzing components used in-service, our approach provides a unique strategy to estimate the mechanical properties under operational conditions.

Fig. 13 further demonstrates the potential to integrate the computational approach to the selection and design of materials. A modest increase in fracture energy of the TGO interface to reach 50 Jm^{-2} (equivalent to 1.8 MPa $m^{1/2}$) would reduce the delamination length by 50% from 120 μm to 60 μm. Furthermore, an increase of fracture energy of the TGO interface above 70 Jm^{-2} or 2.0 MPa $m^{1/2}$ would result in no delamination at the alumina interface estimated from Fig. 13, and this value can be considered as the optimal fracture toughness value for TBC design.

The TC Young's modulus also plays an important role in interface toughness and a TC bottom layer near the substrate with high Young's modulus is desirable as well for increasing FOD resistance. In this case, a stronger, tougher, and dense YSZ bottom layer in TC would also be helpful to increase the alumina interface toughness. These findings have confirmed the dependence of interface delamination on the alumina fracture stress, energy release rate (fracture energy), and Young's modulus of TC as reported in the existing literature [13,20,26].

4. Conclusions

This paper integrates experiments with 2D and 3D finite element models that explicitly represent the microstructure of TBC to simulate the damage induced by the impact of foreign objects. Crack-dependent parameters were adjusted to match crack morphology and length observed in experiments. In this way, material parameters such as fracture stress and energy release rate of the TBC were identified, from which the fracture toughness of TC and alumina interface are calculated.

The analysis estimated material properties independently and assessed model input sensitivities. Best estimates of material parameters informed models to predict localized damage at kink bands and estimate the interface delamination. In terms of the TBC samples, the fracture toughness of TC was estimated to be around 0.1 MPa $m^{1/2}$ to 0.5 MPa $m^{1/2}$ and the fracture toughness of the TGO interface was about 1.5 MPa $m^{1/2}$ to 1.7 MPa $m^{1/2}$. These ranges derived from models agree with the values reported in the literature for similar materials.

Our analysis also determined that a TGO with a fracture toughness above 2.0 MPa $m^{1/2}$ would not delaminate under the service conditions replicated in the erosion test. This modeling approach can be used to design novel TBC by optimizing microstructure, micro-porosity, column

size, inter-column friction, and yield strength.

The novel integrated computational approach of material engineering enables a simple characterization of TBC toughness under service conditions and offers great potential to support the design of novel TBC systems. Compared to the conventional experimental methods, using the integrated approach is also more cost-effective and less time-consuming. The approach can also be employed to design the composition and microstructure of TBCs and advance erosion-resistant systems for next-generation coatings.

Declaration of competing interest

The authors declare that they have no known competing financial interests or personal relationships that could have appeared to influence the work reported in this paper.

References

[1] R.G. Wellman, J.R. Nicholls, A review of the erosion of thermal barrier coatings, J. Phys. Appl. Phys. 40 (16) (2007), https://doi.org/10.1088/0022-3727/40/16/R01. Available at.

[2] M. Watanabe, C. Mercer, C.G. Levi, A.G. Evans, A probe for the high-temperature deformation of thermal barrier oxides, Acta Mater. 52 (6) (2004) 1479–1487, https://doi.org/10.1016/j.actamat.2003.11.029. Available at:.

[3] D. Zhu, J.A. Nesbitt, C.A. Barrett, T.R. McCue, R.A. Miller, Furnace cyclic oxidation behavior of multicomponent low conductivity thermal barrier coatings, J. Therm. Spray Technol. 13 (1) (2004) 84–92, https://doi.org/10.1361/10599630418185. Available at:.

[4] M. Frommherz, A. Scholz, M. Oechsner, E. Bakan, R. Vaßen, Gadolinium zirconate/YSZ thermal barrier coatings: mixed-mode interfacial fracture toughness and sintering behavior, Surf. Coating. Technol. 286 (2016) 119–128, https://doi.org/10.1016/j.surfcoat.2015.12.012. Available at:.

[5] X. Wang, C. Wang, A. Atkinson, Interface fracture toughness in thermal barrier coatings by cross-sectional indentation, Acta Materialia. Acta Materialia Inc. 60 (17) (2012) 6152–6163, https://doi.org/10.1016/j.actamat.2012.07.058. Available at:.

[6] J. Krishnasamy, S.A. Ponnusami, S. Turteltaub, S. van der Zwaag, Computational investigation of porosity effects on fracture behavior of thermal barrier coatings, Ceramics International. Elsevier Ltd and Techna Group S.r.l. 45 (16) (2019) 20518–20527, https://doi.org/10.1016/j.ceramint.2019.07.031. Available at:.

[7] S.T. Kyaw, I.A. Jones, T.H. Hyde, Simulation of failure of air plasma sprayed thermal barrier coating due to interfacial and bulk cracks using surfacebased cohesive interaction and extended finite element method, J. Strain Anal. Eng. Des. 51 (2) (2016) 132–143, https://doi.org/10.1177/0309324715615746. Available at:.

[8] J.R. Nicholls, Y. Jaslier, D.S. Rickerby, Erosion and foreign object damage of thermal barrier coatings, Mater. Sci. Forum 251– 254 (PART 2) (1997) 935–948, https://doi.org/10.4028/www.scientific.net/msf.251-254.935. Available at:.

[9] J.R. Nicholls, Y. Jaslier, D.S. Rickerby, Erosion of EB-PVD thermal barrier coatings, Mater. A. T. High. Temp. 15 (1) (1998) 15–22, https://doi.org/10.1080/09603409.1998.11689572.

[10] J.R. Nicholls, R.G. Wellman, M.J. Deakin, Erosion of thermal barrier coatings, Mater. A. T. High. Temp. 20 (2) (2003) 207–218, https://doi.org/10.1179/mht.2003.024. Available at:.

[11] R.G. Wellman, J.R. Nicholls, Erosion, corrosion and erosion-corrosion of EB PVD thermal barrier coatings, Tribol. Int. 41 (7) (2008) 657–662, https://doi.org/10.1016/j.triboint.2007.10.004. Available at:.

[12] R.G. Wellman, M.J. Deakin, J.R. Nicholls, The effect of TBC morphology and aging on the erosion rate of EB-PVD TBCs, Tribol. Int. 38 (9 SPEC. ISS.) (2005) 798–804, https://doi.org/10.1016/j.triboint.2005.02.008. Available at:.

[13] X. Chen, R. Wang, N. Yao, A.G. Evans, J.W. Hutchinson, R.W. Bruce, Foreign object damage in a thermal barrier system: mechanisms and simulations, Mater. Sci. Eng. 352 (1–2) (2003) 221–231, https://doi.org/10.1016/S0921-5093(02)00905-X. Available at:.

[14] M. Watanabe, T. Xu, C.G. Levi, A.S. Gandhi, A.G. Evans, Shear band formation in columnar thermal barrier oxides, Acta Mater. 53 (13) (2005) 3765–3773, https://doi.org/10.1016/j.actamat.2005.04.029. Available at:.

[15] X. Chen, J.W. Hutchinson, Particle impact on metal substrates with application to foreign object damage to aircraft engines, Journey of the Mechanics and Physics of Solids 50 (2002) 2669–2690. Available at: 10.1016/S0022-5096(02)00022-4.

[16] J.M. Wright, D.C. Faucett, M. Ayre, Phenomena of foreign object damage by spherical projectiles in EB-PVD thermal barrier coatings of turbine airfoils, J. Eng. Gas Turbines Power 136 (2014), https://doi.org/10.1115/1.4027362. Available at.

[17] Q.M. Yu, Q. He, F.L. Ning, Influence of interface morphology on erosion failure of thermal barrier coatings, Ceram. Int. 44 (17) (2018), https://doi.org/10.1016/j.ceramint.2018.08.188, 21349–57.

[18] W. Zhu, Y.J. Jin, L. Yang, Z.P. Pi, Y.C. Zhou, Fracture mechanism maps for thermal barrier coatings subjected to single foreign object impact, Wear 414–415 (2018), https://doi.org/10.1016/j.wear.2018.08.020, 303–9.

[19] M. Matsuzawa, M. Abe, S. Horibe, Strain rate dependence of tensile behavior and environmental effect in zirconia ceramics, ISIJ Int. 43 (4) (2003) 555–563, https://doi.org/10.2355/isijinternational.43.555. Available at:.

[20] X. Chen, M.Y. He, I. Spitsberg, N.A. Fleck, J.W. Hutchinson, A.G. Evans, Mechanisms governing the high-temperature erosion of thermal barrier coatings, Wear 256 (7–8) (2004) 735–746, https://doi.org/10.1016/S0043-1648(03)00446-0.49. Available at:.

[21] R. G, W.H. Cook, A constitutive model and data for metals subjected to large strains, high strain rates and high temperature, Proceedings of the 7th International Symposium on Ballistic 21 (1) (1983) 541–547.

[22] J. Lankford, W.W. Predebon, J.M. Staehler, G. Subhash, B.J. Pletka, C.E. Anderson, The role of plasticity as a limiting factor in the compressive failure of high strength ceramics, Mech. Mater. 29 (3–4) (1998) 205–218, https://doi.org/10.1016/S0167-6636(98)00023-4. Available at:.

[23] M. Schutze, Protective Oxide Scales and Their Breakdown, WILEY, 1997. Available at: www.wiley.com/en-gb/Protective+Oxide+Scales+and+Their+Breakdown-p-9780471959045.

[24] G. Honite, Blast media data sheet. Guyson, Available at: https://www.guyson.co.uk/aftersales/guyson-blast-media/glass-blast-media. (Accessed 13 February 2023).

[25] B.A. Latella, T. Liu, High-temperature young's modulus of alumina during sintering, J. Am. Ceram. Soc. 88 (3) (2005) 773–776, https://doi.org/10.1111/j.1551-2916.2005.00082.x. Available at:.

[26] D.R. Mumm, G.A. Evans, Mechanisms controlling the performance and durability of thermal barrier coatings, Key Eng. Mater. 197 (2001) 199–230, https://doi.org/10.4028/www.scientific.net/kem.197.199. Available at:.

[27] T. Czeppe, S. Wierzbinski, Structure and mechanical properties of NiAl and Ni3Al-based alloys, Int. J. Mech. Sci. 42 (8) (2000) 1499–1518, https://doi.org/10.1016/S0020-7403(99)00087-9. Available at:.

[28] G.K. Dey, Physical metallurgy of nickel aluminides, Sadhana - Academy 51 Proceedings in Engineering Sciences 28 (1–2) (2003) 247–262, https://doi.org/10.1007/BF02717135. Available at:.

[29] N.A. Fleck, Th Zisis, The erosion of EB-PVD thermal barrier coatings: the competition between mechanisms, Wear 268 (11) (2010), https://doi.org/10.1016/j.wear.2009.12.020, 1214–24.

[30] M. Benachour, Effect of the amplitude loading on fatigue crack growth, Procedia Eng. 2 (2010) 121–127.

[31] Y. Xing, Q. Wei, J. Hao, The fracture toughness of alumina coatings plasma-sprayed at different in situ temperatures, Ceram. Int. 38 (2012) 4661–4667, https://doi.org/10.1016/j.ceramint.2012.02.048. Available at.

2023-05-15

Estimation of thermal barrier coating fracture toughness using integrated computational materials engineering

Geng, Xibo

Elsevier

Geng X, Wellman R, Isern Arrom L, et al., (2023) Estimation of thermal barrier coating fracture toughness using integrated computational materials engineering. Ceramics International, Volume 49, Issue 15, 1 August 2023, pp. 25788-25794

https://doi.org/10.1016/j.ceramint.2023.05.124